Strain localisation and grain breakage in sand under shearing at high mean stress: insights from in-situ x-ray tomography

M. Gkiousas-Kapnisis, A. Totabi, Gioacchino Cinno Viggiani, E. Ando, Reza Alikarami

▶ To cite this version:

M. Gkiousas-Kapnisis, A. Totabi, Gioacchino Cinno Viggiani, E. Ando, Reza Alikarami. Strain localisation and grain breakage in sand under shearing at high mean stress: insights from in-situ x-ray tomography. Acta Geotechnica, Springer Verlag, 2015, 10 (1), pp.15-30. 10.1007/s11440-014-0364-6 . hal-01954512

HAL Id: hal-01954512
https://hal.univ-grenoble-alpes.fr/hal-01954512

Strain localisation and grain breakage in sand under shearing at high mean stress: insights from *in-situ* x-ray tomography

Alikarami R.[1,2], Andò, E.[3], Gkiousas-Kapnisis M.[3], Torabi A.[1], Viggiani G.[3]

[1] Uni CIPR, Uni Research , P.O. Box 7810, N-5020 Bergen, Norway

[2] Earth Science Departments, University of Bergen, P.O. Box 7800, N-5020 Bergen, Norway

[3] Grenoble-INP / UJF-Grenoble 1 / CNRS UMR 5521, Laboratoire 3SR, 38041 Grenoble, France

Corresponding author: Reza Alikarami, Uni CIPR, Uni Research , P.O. Box 7810, N-5020 Bergen, Norway (reza.alikarami@uni.no)

Abstract

This work presents results from a series of triaxial compression tests on two quartz sands (differing principally in grain shape), at confining pressures high enough to cause grain breakage during shearing. Tests are performed inside an x-ray scanner, which allows specimens to be imaged non-destructively as they deform. Observation of the acquired images clearly shows different mechanisms of deformation, including shearing, dilation, compaction and grain breakage. These mechanisms are investigated quantitatively through 3D measurements of local porosity, as well as strain (obtained by 3D Digital Image Correlation), which is analysed in terms of volumetric and shear components. These tools allow the transition between macroscopically dilative (typically of a dense sand at low mean stress) and compactive behaviour to be investigated. The analysis reveals that at the high end of the confining pressure range studied (100 to 7000 kPa) the more rounded sand deforms with highly localised shear and volumetric strain – the porosity fields show a dilative band within which a compactive region (due to grain crushing) grows. The more angular material shows shear strain localisation, however its faster transition to compactive behaviour (due to a higher propensity for individual grains to crush) translates to much more distributed compactive volumetric strain.

Keywords

Deformation band, Grain breakage, Grain shape (angularity), Triaxial compression test, In-situ x-ray microtomography, 3D Digital Image Correlation

1. Introduction

Weakly cemented and poorly lithified sandstones are important class of geological reservoirs for hydrocarbon production and are good candidates for geological carbon dioxide sequestration due to their high porosity and permeability. These highly porous rocks undergo different modes of deformation depending on their stress history as well as their lithological and petrophysical properties. Strain in such sandstones may localise into thin (mm-scale) planar structures often referred to as deformation bands [1-3]. The kinematics of deformation bands always includes shear, while the volumetric response ranges from dilative to compactive strain (e.g. [1, 4]). Both porosity and permeability are reduced within compaction bands and compactive shear bands, as a result of pore-collapse and possible grain breakage [5-7]. In dilative shear bands, porosity increases and (depending on pore tortuosity and changes in specific surface area) permeability may decrease or increase [8-10]. Extensive experimental work has been carried out to study the effects of variables such as stress level, porosity and grain size on localised deformation in well lithified and cemented sandstone (e.g. [11-15]).

At the micro-scale (i.e. the scale of the grain, for a sandstone), strain corresponds to combinations of different mechanisms including grains rearrangement (sometimes referred to as “particulate flow”), grain breakage (cataclasis) and cement breakage. A full understanding of strain localisation in sandstones requires investigation of these mechanisms, all of which strongly depend on grain shape and angularity. Experience and knowledge from our previous work on natural compactive shear bands formed in very porous and friable sandstone (e.g., [16, 17]) were the motivation to explore the behaviour of sand at high mean stress. In this paper, sand is adopted as a model material that allows the investigation (at substantially lower mean stresses than that needed for sandstone) of all deformation mechanisms mentioned above at the grain scale – with the exception of cement breakage.

X-ray tomography is proving to be an ideal tool for the investigation of the micro-mechanisms of deformation in sand – for example recent work from Laboratoire 3SR, Grenoble, has clearly demonstrated the effect of grain angularity on the macroscopic mechanical behaviour of sand as well its effect on the formation and development of shear bands in different types of sand [18-20], all this at relatively low mean stress, which rules out grain breakage.

A series of dry triaxial compression tests on two different sands has been performed *in-situ* (*i.e.* performing x-ray scans at various points throughout loading) inside the x-ray scanner in Laboratoire 3SR (Grenoble), at mean stresses up to 7000 kPa – which proves to be high enough to cause grain breakage. The two sands tested are both quartz sands, with similar grain size distributions but different angularities: Ottawa 50-70 sand (rounded) and Hostun HN31 sand (angular).

The structure of the paper is as follows: the materials and testing method are first described; this is followed by a description of the tests performed. The typical, macroscopic measurements obtained from triaxial testing are detailed for all tests. The image processing tools used to make micro-scale measurements on the acquired x-ray images are then briefly described. These measurements are further used to explain the differences in the macroscopic responses observed. The paper closes with a discussion of the results obtained.

2. Experiments

2.1 Materials tested

The two different types of sand tested in this work are Hostun HN31 sand and Ottawa 50-70 sand. Hostun sand is angular siliceous sand (see SEM image in Fig. 1) produced in a quarry close to the commune of Hostun in the Rhône-Alpes region of France. The Hostun HN31 sand studied in this work [21] is mechanically identical to the “Hostun S28” and “Hostun RF” varieties that have been thoroughly studied (e.g. [22]). The Ottawa sand is a rounded siliceous sand (see SEM image in Fig. 1), that comes from sedimentary deposits in Ottawa, Illinois (U.S.A.). A particle size distribution for both sands is presented in Fig. 2; the values of D_{50} of Hostun and Ottawa sands are 338 µm and 310 µm, respectively.

2.2 Experimental setup and testing campaign

A series of triaxial tests on small specimens of dry Hostun and Ottawa sands at confining pressures ranging from 100 kPa to 7000 kPa have been carried out at Laboratoire 3SR with *in-situ* x-ray scanning. The specimens used in this work are cylinders of approximately 22 mm height and 11 mm diameter, with non-lubricated end platens. Note that from a mechanical standpoint, the response obtained with such small specimens compares well to that obtained with larger (standard size) specimens (in [23]), as discussed in detail in [24].

The triaxial cell has no steel tie-bars to take the return force from the axial compression of the specimen; this is instead taken by the cell in tension (see Fig. 3). The absence of steel tie-bars allows the specimen to be imaged by x-rays, without disturbance, inside the cell. Two triaxial cells were used in this experimental campaign: a high and a low pressure cell, which differ principally in the thickness of the wall of the cell, as well as how the confining pressure is applied. Both cells are made of PMMA (Plexiglas) which is transparent to visible light as well as to x-rays. In the lower pressure cell shown in Fig. 3 (designed for confinements up to 1000 kPa), the confining fluid is water, and confining pressure is applied by compressed air (coming from a compressor) with a pressure controller, allowing a fine control of the confining pressure. For the higher pressure cell, confinement by air is no longer feasible, and so a pump is used; for compatibility with the pump, the confining fluid is oil.

Given the different confining pressures and fluids, two different membranes have been used in this experimental campaign. In the lower pressure tests, a 300 μm thick latex membrane (very transparent to x-rays) is used. In the higher pressure tests, however, a 500 μm thick neoprene membrane is used – primarily to avoid piercing of the membrane, but also for compatibility with the confining fluid. The x-ray absorption of this membrane is considerably higher than the latex one, so it is clearly visible in the images coming from x-ray tomography (see Fig. 6).

All specimens are prepared by air pluviation into the membrane stretched in a mould, aiming for a dense initial packing (this specimen preparation technique has been selected for its reproducibility). Once prepared, samples are installed into the triaxial cell with vacuum applied to the sample. The cell is then filled with the relevant confining fluid, which is slowly pressurised to an initial isotropic state, while the vacuum is released.

Each specimen is loaded isotropically until the desired confining pressure is reached, at which point deviatoric loading is applied under strain control by shortening the sample axially using a domed ram driven up by the loading system. The force required to advance the ram is recorded with a load cell, and the displacement of the ram is recorded with an LVDT. The specimen is shortened with a displacement rate of 21 μm per minute (corresponding to a nominal strain rate of just under 0.1% per minute).

At various key points during a test, loading is halted, and a tomographic scan is performed by acquiring 1024 x-ray radiographs of the sample as it is rotated 360° around its vertical axis by the rotation stage visible in Fig. 3. Since the specimens scanned are relatively small, the geometrical zoom provided by the x-ray cone-beam coming from the generator gives a pixel size of 15.6 µm/pixel, meaning that each grain within the specimen (we recall the D_{50} is bigger than 300 µm for both sands) is clearly represented. The set of radiographs acquired is then reconstructed (using DigiCT 2.4.2 from Digisens) into a 3D field of the x-ray attenuation inside the specimen.

3. Macroscopic results of triaxial testing

This section presents the macroscopic results coming from the triaxial compression tests analysed in this work (see Table 1).

Table 1. Summary of tests analysed in this paper

Material	Test Name	Confining Pressure	Initial Porosity (before shearing)
Ottawa	OUEA06	100 kPa	32.1%
Ottawa	OHEA03	4000 kPa	29.1%
Ottawa	OHEA01	7000 kPa	27.3%
Ottawa	OHEA02	7000 kPa	28.9%
Hostun	HNEA01	100 kPa	37.7%
Hostun	HHEA03	1000 kPa	33.7%
Hostun	HHEA05	1000 kPa	34.8%
Hostun	HHEA04	2000 kPa	35.1%
Hostun	HHEA06	3000 kPa	34.3%
Hostun	HHEA02	4000 kPa	34.6%
Hostun	HHEA01	7000 kPa	33.8%

In some tests, a few scans are performed during the isotropic loading of the specimen, however most are during deviatoric loading. When deviatoric loading is halted to perform a scan, some axial stress relaxation occurs, which can be seen as small drops of deviator stress throughout the q/p *vs*. ε_a responses of both sands (see Figs. 4 and 5 noting that $p = \frac{1}{3}(\sigma_a + 2\sigma_r)$ and $q = (\sigma_a - \sigma_r)$ with σ_a and σ_r being the axial and radial stresses respectively).

Figures 4 and 5 show the deviator stress response normalised by the mean normal stress (q/p) and volumetric strain response (in %) both against axial shortening (normalised by the initial height) for all the tests on Ottawa and Hostun sands. Since samples are tested dry, the macroscopic measurement of bulk specimen volume that is used to measure volumetric strain is actually derived from the images of the specimen – the technique for making this measurement is detailed in Section 4.1.

It is clear from the responses shown for both sands that there is a significant, but progressive change between the macroscopic material response at 100 kPa and 7000 kPa confinements. The triaxial compression behaviour of Ottawa sand (shown in Fig. 4) with increasing mean stress reveals a progressive retardation (with respect to axial shortening) of the peak deviatoric stress as well as a progressive reduction of its value. The difference between the peak deviator stress and the plateau is large at low confinement (test OUEA06), and the difference reduces with increasing confining pressure – as does the normalised q/p value of the plateau. The considerable dilation undergone by the specimen at 100 kPa confinement progressively reduces from 4000 to 7000 kPa. Although the volumetric strain curves obtained for the two tests performed at 7000 kPa confinement differ, the response can be seen to be slightly dilatant (compared to test OUEA06 at 100 kPa) in both cases.

The evolution of the mechanical response of Hostun sand (Fig. 5) with increasing confining pressure has the same sort of evolution as with the Ottawa sand described above (less clear peak stress and increasingly less dilatant behaviour), however, over the same range of confining pressures this evolution appears to be considerably more rapid: a peak in deviator stress is only clearly visible until 3000 kPa confinement – at higher confinement there is no peak, only strain hardening. The volumetric response also displays a good deal more change than for Ottawa sand: the specimen tested at 100 kPa confinement shows clear dilatancy, whereas the one tested at 7000 kPa confinement is contractant throughout. The other tests at 1000, 2000, 3000 and 4000 kPa fall in between these two cases. The stress response of HHEA05 (1000 kPa confinement) also reveals a clear peak, yet with a lower dilatancy than HNEA01 at 100 kPa confinement. Stress-strain responses of HHEA04 at 2000 kPa and HHEA06 at 3000 kPa confinement also show peaks but not as clearly marked as for HNEA01 and HHEA05. Their volumetric responses are very slightly dilatant in the case of HHEA04, and slightly contractant for HHEA06. Stress-strain response of sample HHEA02 tested at 4000 kPa confinement reveals no peak, and shows contraction, but to a lesser extent than test HHEA01 at 7000 kPa.

During the post-test removal of specimens tested at high pressures, the production of fines was noted when the contents of the membrane was emptied for weighing. The production of fines by grain breakage may well explain the change from dilation to compaction in the macro-scale volumetric responses of these sands (see Figs. 4 and 5).

4. Image analysis

This section briefly outlines the image analysis techniques used to make micro-scale measurements on the various 3D images coming from the tomographic scans during loading. The objective is to use these tools to explain the differences in the macroscopic responses detailed above. The 3D images coming from tomography are 16-bit greyscale measuring 1250x1250x1600 pixels, with a pixel size of 15.6 µm.

4.1 Preparation of images for analysis

In order to make micro-scale measurements from the acquired images, the first step is to define the domain (within the image) of the solid skeleton to be analysed, so that measurements are made only on this part of each image, and that other objects (such as the top and bottom platens, as well as the neoprene membranes) are not taken into account. The specimen-platen interface is considered to be a plane, which can be tilted with respect to the specimen's axis. Given that the platens have a long extent of flat greyscale (as opposed to the sample, which is made of grains and pores), this information is incorporated into an automatic procedure which automatically detects points on this interface and fits a plane to the two specimen-platen interfaces.

The shape of the membrane is rendered more complex by the fact that it does not necessarily have a uniform thickness (especially once the sample starts to undergo localised deformation); consequently, there is no question of manually removing the membrane, especially taking into account the large number of 3D images acquired. A specific image processing technique is therefore developed to recognise the inner surface of the membrane: for each horizontal slice, 300 equally-spaced radial profiles are made, centred on the approximate axis of the specimen. As illustrated in Fig. 7, the plot of the variance of this profile reveals sharp peaks, corresponding to the rapidly changing greyscale values at material interfaces. Each greyscale profile is variance filtered and the characteristic peaks are used to identify the border points: a closed border defining the inside of the membrane is then created by connecting these 300 individual points by linear segments. Finally, a 3D median filter (of radius 5 pixels) is used to smooth out this border.

The full technique is shown in Fig. 7, and its effectiveness can be seen from the way in which the membrane visible in Fig. 6b is removed in Fig. 6c.

After each individual stage has been processed, the inside of the specimen is defined with a geometrically complex border around the inside of the membrane bounded by two planes. The number of voxels (3D pixels) within this space can be counted, using the pixel size, and used to calculate the bulk volume of the specimen as imaged.

4.2 Local measurement of porosity

Porosity is a key measurement for granular materials, and its spatial distribution is of particular interest given the different volumetric strain responses seen with macro-scale measurements. Porosity is defined as the ratio of the volume of voids to the total volume. This can be measured locally, by defining a 3D subvolume within a 3D image and measuring the volume of the voids within the subvolume. In previous work [26], voids have been counted by *binarising* the greyscale 3D image into a black and white image of the solid and void phases by applying a threshold. Observation of the images obtained in this work, particularly for Hostun sand at high confining pressure and after shearing shows that grain breakage does indeed occur (see Fig. 15 for example), and that the finer grains produced can be small compared to the pixel size of the images. This smaller grain phase partially fills voxels, and consequently looks like a homogeneous material of x-ray attenuation in between grain and void, thus invalidating the inherent two-phase hypothesis for binarisation. In this work, the volume of voids in each subvolume is calculated on the greyscale (as opposed to binary) 3D images; values of pore and grain greyscale are measured manually on a small selection of pores and grains throughout the specimen. Any voxel having a greyscale value equal to, or higher than, the grain greyscale value identified is 100% solid, and any voxel having a greyscale value equal to, or lower than, the pore greyscale value identified is 100% pore. Greyscale values between these two greyscale limits are interpolated with a linear relationship.

Local measurements of porosity are therefore made by defining local subvolumes, centred on a number of regularly spaced nodes. The size of the cubic subvolumes is selected as a reasonable trade-off between sensitivity and representativity of the measurement. Subvolume sizes of 620x620x620 μm and 470x470x470 μm are used to make measurements on Hostun and Ottawa sand respectively.

4.3 Digital Image Correlation (DIC)

In order to make measurements of local kinematics between two 3D images of a deforming specimen, Continuum Digital Image Correlation, as implemented in Tomowarp by Hall [27], has been used to follow regularly-distributed cubic subvolumes between two different greyscale images. The method relies on image correlation and attempts to find a pattern (i.e. the greyscale inside a given subvolume) extracted in the reference configuration, and looks for this pattern in the deformed configuration. When the best matching pattern is found (by optimizing a correlation coefficient mapping one image to the other), the displacement of the subvolume is a natural output, and is measured to subpixel precision. This gives the displacement of a series of points spread throughout the reference configuration, giving therefore, a full-field measurement of the kinematics between the two states. By deriving this displacement field, the 3D strain tensor can be obtained. The first two invariants of the strain tensor (representing volumetric and shear strain) are chosen for display in the results shown in Section 5.

Image correlation has an increased probability of making matching errors when a considerable amount of grain breakage occurs between steps. This is due to the considerably different patterns from one image to another that naturally make the patterns harder to match. In order to minimize these potential errors, small increments are analyzed in this work. It is worth noting that DIC is used incrementally, i.e. to measure the displacement field from image i-1 to image i, rather than from the initial configuration up to image i. This is different from the “total” porosity measurements presented in Section 5.

5. Measurements from image analysis

5.1 Tests on Ottawa sand

This section uses the 3D images acquired during the different tests on Ottawa sand to investigate the micro-mechanisms at play during triaxial shearing of the specimens tested at 100, 4000 and 7000 kPa confining pressure.

Figure 8 shows vertical slices from the final states imaged in each test on Ottawa sand analysed in this work. The slices are oriented to contain the axis of the sample and the normal to the single shear band that is apparent in all cases. In all images acquired at high pressure, the membrane and platens have been removed using the technique described in Section 4.1. These images reveal that in OUEA06 a clear dilatant shear band crosses the sample, whereas for the two samples tested at 7000 kPa confinement, a narrow compactive shear band is also visible, containing crushed material. OHEA03 is an intermediate case, i.e. with no change or slight change in porosity inside the shear band.

Figure 9 shows the porosity maps obtained for some key steps during the triaxial shearing of three of the specimens. Prior to shearing, all specimens have relatively uniform distribution of porosities ranging from n=27% to n=32%. Specimen OUEA06 (tested at 100 kPa confinement) presents a clear, dilatant shear band that develops early in the test – at 3.9% axial shortening (around the position of the peak stress) localised dilation is visible, with a porosity in the band of around n=46% by the end of the test. OHEA03 (4000 kPa) does not seem to show localised changes in porosity at 3.9% axial strain, however around its peak (at 7.7% shortening, which is considerably later than OUEA06), localised dilation is visible. This dilative band continues to develop with increasing shearing, and becomes more pronounced by the end of the test (reaching a value of n=39%). The sample tested at 7000 kPa confinement (OHEA01) has a considerably different behaviour, which is captured well by looking at the porosity maps: by the end of the test, a band of *reduced* porosity is noticeable, reaching n=33% (2% lower than the surrounding material). Looking back towards the beginning of the test, two mechanisms can be seen: there is a clear and relatively uniform densification of the sample between 0 and 4.3% shortening. Thereafter, a dilatant shear band is visible at 12.9% shortening (achieving a porosity of n=36%), and at 14.3% shortening, *within* this *dilatant* band, a zone of contraction starts to develop at the bottom of the band (on the right side of the specimen), and appears to progressively develop within the dilatant band as shearing continues: by 17.2% shortening it crosses the entire specimen. This contractive band is consistent in space with the zone of crushed material visible in Fig. 8.

Figure 10 shows the DIC results (vertical sections of the calculated fields of volumetric and shear strain) for some selected increments of the three tests analysed. Interestingly, incremental volumetric strain fields can reveal mechanisms that changes in total porosity simply are not sensitive enough to pick up. While over the peak the volumetric strain fields from DIC merely confirm the dilating bands shown by the porosity fields, the increments analysed at the end of the tests reveal that as shearing continues, the volumetric strain in the bands of localised shear strain either disappears (for the test at lowest confinement) or becomes compactive (in all the other tests), likely due to grain breakage. The shear strain fields show that in all tests the shear band gets thinner after the peak.

5.2 Tests on Hostun sand

Figure 11 shows vertical slices from the final states imaged in each test on Hostun sand analysed in this work. The slices are oriented to contain the axis of the sample and the normal to the single shear band (when this is apparent).

As for Ottawa, in all images acquired at high pressure, the membrane and platens have been removed using the technique described in Section 4.1. These images reveal a range of final states that go from a high porosity band (at 100 kPa and to a lesser extent at 1000 kPa confinement) to a wide band with clear evidence of crushed grains (in the tests at 4000 and 7000 kPa). The tests at 2000 kPa and 3000 kPa confinement are intermediate cases, with no striking changes in porosity throughout the specimen.

Figure 12 shows the porosity maps obtained for some key steps during the triaxial shearing of the specimens of Hostun sand. Prior to shearing, all specimens have relatively uniform distribution of porosities ranging from n=27% to n=32%, with initial porosity generally decreasing with increasing confining pressure, as expected. Specimens HNEA01 and HHEA05 both exhibit a clear shear band that becomes increasingly dilatant with increasing shortening – with the out-of-band material remaining at almost constant porosity. Specimen HHEA04 tested at 2000 kPa confinement seems to deform with essentially no porosity change. A progressive and distributed reduction in porosity is evident in all specimens tested at higher cell pressure. Specimen HHEA02 shows some degree of localisation in porosity reduction at the end of the test.

Figure 13 shows the DIC results (vertical sections of the calculated fields of volumetric and shear strain) for some selected increments of the three lower pressure tests. At 100 kPa and 1000 kPa confinement, (shear and volumetric) strain localisation starts in a wide band and then progressively concentrates with increasing axial shortening. At 2000 kPa, the shear strain concentrates in a similar fashion, while the maps of incremental volumetric strain confirm that little or no volume changes occur during (progressively localised) shearing. The DIC results for the other three tests analysed (shown in Fig. 14) show that a shear band eventually forms in all tests – which was not evident from either x-ray images or the porosity maps. The reason for this can be seen in the volumetric strain increments presented, which show no localisation. It is also important to note that at these levels of confinement, volumetric strain is essentially compactive rather than dilative – consistent with the global volumetric strains shown in Fig. 5.

6. Discussion and conclusions

The range of cell pressures used in this experimental campaign has resulted in a significant evolution of the mechanical response of both tested sands, at the macroscopic level. The tendency for increasing confinement is for the volumetric response to change from dilative to contractive, and for the peak of the deviator stress to become less pronounced. This is entirely consistent with previous experimental findings (e.g. [28-30]), all of which attribute this change in macroscopic behaviour to the appearance of grain crushing with increasing mean stress – which is supported by post-mortem sieve analyses.

Grain crushing is generally studied through its numerous effects at the macro scale (e.g. its effect on compressibility, shear strength, permeability, etc.). In this work, the process of grain crushing is approached experimentally at the scale of the grain. X-ray micro tomography allows imaging of this process, which is a major mechanism of inelastic deformation in sand at high pressure – along with granular rearrangement. Furthermore, the comparison of successive pairs of x-ray images (with 3D DIC) yields 3D (incremental) strain fields, which reveal the nature of the strain occurring between the two states.

In all the tests performed on Ottawa sand, shear strain and volumetric strain are observed to localise into a band a few grains thick. At high pressure, grain crushing only occurs in the shear band when a sufficiently high porosity is reached. It should be mentioned that this evolution is well portrayed by the first three stages (dilation, pore collapse and grain size reduction) in the sequence suggested by Lothe *et al*. [30] to describe the evolution of deformation bands in sandstones.

DIC measurements in Hostun sand show that while shear strains localise in a shear band at all pressures, volumetric strain is localised when dilatant (at low pressures) and becomes increasing less localised in the contractive regime. X-ray images show diffuse breakage at high pressure, with the relatively wide regions of porosity reduction corresponding in space to regions of crushed grains (see Fig. 15).

Since both Ottawa and Hostun are quartz sands with similar grain size distribution, the cause of their different responses can be mainly ascribed to the shape of their grains (rounded in the former and angular in the latter). One may hypothesise that in the more angular material the amount of energy required to break a grain is lower due to the presence of sharper contacts that concentrate stresses on the grain. Therefore, for a given stress level one would expect more crushing in the angular material – which is exactly what is observed. The massive grain crushing observed in Hostun sand at 7000 kPa confinement suggests that the material is close to the stress conditions required for distributed grain breakage. In Ottawa sand, even at 7000 kPa confinement breakage only occurs after a strong reduction of porosity, which for a given stress increases interparticle forces – this happens only inside the narrow compactive shear band of localised strain (see Fig. 15). These differences manifest themselves in the macroscopic response of the two sands, most evidently in their volumetric response – with the specimens of Ottawa sand never showing overall compaction whereas Hostun crosses this threshold between 2000 and 3000 kPa confinement.

The findings of this study on sand highlight the central role played by grain shape on both the stress level needed to break grains as well as the patterns of deformation (localised *vs.* diffuse). It is the authors’ contention that these findings are also largely applicable to poorly lithified sandstones. These results are of particular interest for hydrocarbon production and CO_2 storage in sandstone, where the overall reservoir permeability and its evolution is key for the rate at which extraction/injection processes can occur. In the triaxial compression tests analysed in this work, similar materials differing only by the shape of their grains exhibited very different distributions of particle breakage, diffuse in the angular material and highly localised in the rounded one – with obvious implications for the permeability and its directional variation. The stress paths encountered in a natural reservoir are clearly quite different from triaxial compression, however one might expect grain shape to play an equally important role under any deviatoric stress path, such as those induced by oil production or CO_2 injection.

Acknowledgments

This study is part of the IMPACT Project, a consortium R&D project 207806, at the Centre for Integrated Petroleum Research (Uni CIPR), Uni Research, funded by the Research Council of Norway and Statoil. The authors would like to thank Alessandro Tengattini for his help in the quantitative analysis and interpretation of the test results.

References

1. Schultz RA, Siddharthan R (2005) A general framework for the occurrence and faulting of deformation bands in porous granular rocks. Tectonophysics, 411:1–18. doi: 10.1016/j.tecto.2005.07.008

2. Fossen H, Schultz RA, Shipton ZK, Mair K (2007), Deformation bands in sandstone: A review. J Geol Soc 164:755-769. doi: 10.1144/0016-76492006-036

3. Torabi A, Berg S (2011) Scaling of fault attributes: A review. Mar Pet Geol 28(8):1444-1460. doi: 10.1016/j.marpetgeo.2011.04.003

4. Vajdova V, Baud P, Wong T (2004) Permeability evolution during localized deformation in Bentheim sandstone. J Geophys Res 109:B10406. doi: 10.1029/2003JB002942

5. Antonellini M, Aydin A (1994) Effect of faulting on fluid flow in porous sandstones; petrophysical properties. AAPG Bull 78:355-377.

6. Torabi A, Fossen H, Alaei B (2008) Application of spatial correlation functions in permeability estimation of deformation bands in porous rocks. J Geophy Res 113:B08208. doi: 10.1029/2007JB005455

7. Aydin A, Berryman J (2010) Analysis of the growth of strike-slip faults using effective medium theory. J Struct Geol 32:1629-1642. doi: 10.1016/j.jsg.2009.11.007

8. Cashman S, and Cashman K (2000) Cataclasis and deformation-band formation in unconsolidated marine terrace sand, Humboldt County, California. Geology 28(2):111-114. doi: 10.1130/0091-7613(2000)28<111:CADFIU>2.0.CO;2

9. Du Bernard X, Eichhubl P, Aydin A (2002) Dilation bands: A new form of localized failure in granular media. Geophys Res Letters 29(24):2176. doi: 10.1029/2002GL015966

10. Sulem J, Ouffroukh H (2006) Shear banding in drained and undrained triaxial tests on a saturated sandstone: Porosity and permeability evolution. Int J Rock Mech Min Sci 43:292-310. doi: 10.1016/j.ijrmms.2005.07.001

11. Wong T, David C, Zhu W (1997) The transition from brittle faulting to cataclastic flow in porous sandstone: Mechanical deformation. J Geophys Res 102:3009-302. doi: 10.1029/96JB03281

12. Bésuelle P (2001) Compacting and dilating shear bands in porous rocks: Theoretical and experimental conditions. J Geophys Res 106:13435–13442. doi: 10.1029/2001JB900011

13. Baud P, Klein E, Wong T (2004) Compaction localization in porous sandstones: Spatial evolution of damage and acoustic emission activity. J Struct Geol 26:603-624. doi: 10.1016/j.jsg.2003.09.002

14. Fortin J, Stanchits S, Dresen G, Gue´guen Y (2006) Acoustic emission and velocities associated with the formation of compaction bands. J Geophys Res 111:B10203. doi: 10.1029/2005JB003854

15. Wong T, Baud P (2012) The brittle-ductile transition in porous rock: A review. J Struct Geol 44:25-53. doi: 10.1016/j.jsg.2012.07.010

16. Torabi A (2014) Cataclastic bands in immature and poorly lithified sandstone, examples from Corsica, France. Tectonophysiscs, http://dx.doi.org/10.1016/j.tecto.2014.05.014.

17. Torabi A, Zarifi Z (2014) Energy release rate for propagating deformation bands and their hosted cracks. International Journal of Rock Mechanics and Mining Sciences 67, 184-190.

18. Andò E, Hall SA, Viggiani G, Desrues J, Bésuelle P (2012a) Grain-scale experimental investigation of localised deformation in sand: a discrete particle tracking approach. Acta Geotechnica 7:1-13. doi: 10.1007/s11440-011-0151-6

19. Andò E, Hall SA, Viggiani G, Desrues J, Bésuelle P (2012b) Experimental micromechanics: grain-scale observation of sand deformation. Géotechnique Letters 2:107-112. doi: 10.1680/geolett.12.00027

20. Andò E, Hall SA, Viggiani G, Desrues J (2013) Experimental micro-mechanics of granular media studied by x-ray tomography: recent results and challenges. Géotechnique Letters 3:142-146. doi: 10.1680/geolett.13.00036

21. Sibleco France (2011) Fiche Technique Type HN31. available at: http://www.sibelco.fr/item_img/medias/images/ft12_hn31.pdf

22. Desrues J, Viggiani G (2004) Strain localization in sand: an overview of the experimental results obtained in Grenoble using stereophotogrammetry. Int J Numer Anal Meth Geomech 28(4):279–322. doi: 10.1002/nag.338

23. Colliat-Dangus JL, Desrues J, Foray P (1988) Triaxial testing of granular soi1 under elevated cell pressure. In: Donaghe RT, Chaney RC, and Silver ML (Eds) Advanced triaxial testing of soi1 and rock, ASTM STP 977, American Society for Testing and Materials, Philadelphia, pp 290-310

24. Andò E (2013), PhD Thesis, Experimental investigation of micro-structural changes in deforming granular media using x-ray tomography, Université de Grenoble

25. Kim HK, Santamarina J (2008) Sand–rubber mixtures (large rubber chips). Canadian Geotechnical Journal 45(10):1457–1466. doi: 10.1139/T08-070

26. Hall SA, Bornert M, Desrues J, Pannier Y, Lenoir N, Viggiani G, Bésuelle P (2010) Discrete and continuum analysis of localised deformation in sand using X-ray μCT and volumetric digital image correlation. Géotechnique 60:315–322. doi: 10.1680/geot.2010.60.5.315

27. Hall SA (2006) A methodology for 7D warping and deformation monitoring using time-lapse seismic data. Geophysics 71(4):O21–O31. doi: 10.1190/1.2212227

28. Miura N, Yamanouchi T (1973) Compressibility and drained shear characteristics of a sand under high confining pressures. Technology reports of the Yamaguchi University 1(2):271 -290

29. Zoback MD, Byerlee JD (1976) Effect of high-pressure deformation on permeability of Ottawa sand. AAPG Bulletin 60(9):1531-1542

30. Lothe AE, Gabrielsen RH, Bjørnevoll HN, Larsen T (2002) An experimental study of the texture of deformation bands: effects on the porosity and permeability of sandstones. Petroleum Geoscience 8:195–207. doi: 10.1144/petgeo.8.3.195

Figures

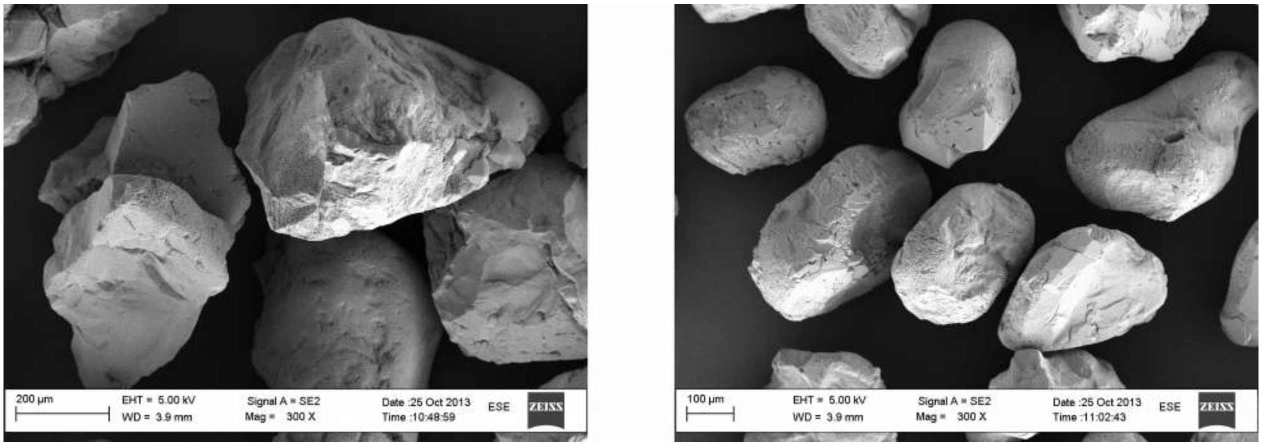

Fig. 1 Scanning Electron Microscope (SEM) images of: left) angular Hostun sand grains, and right) rounded Ottawa sand grains

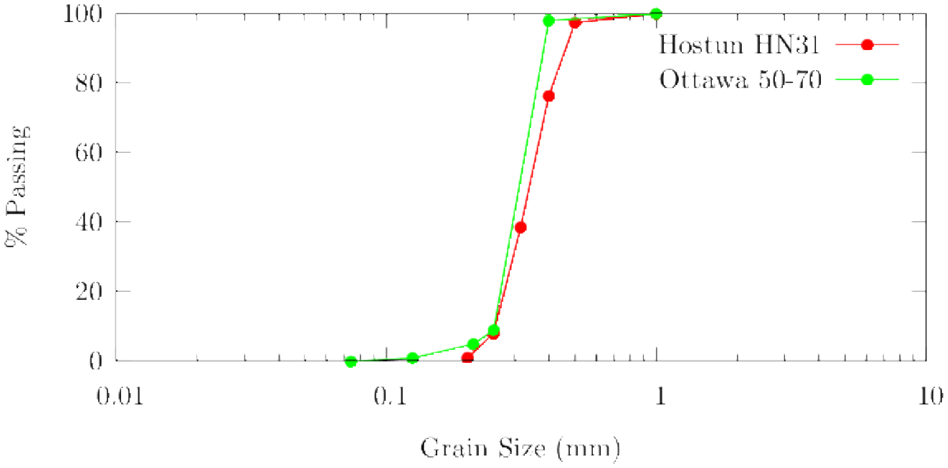

Fig. 2 Grain size distribution curves for the two sands studied in this work. Data for Hostun sand comes from the manufacturer [21], and data for Ottawa sand from Kim and Santamarina [25]

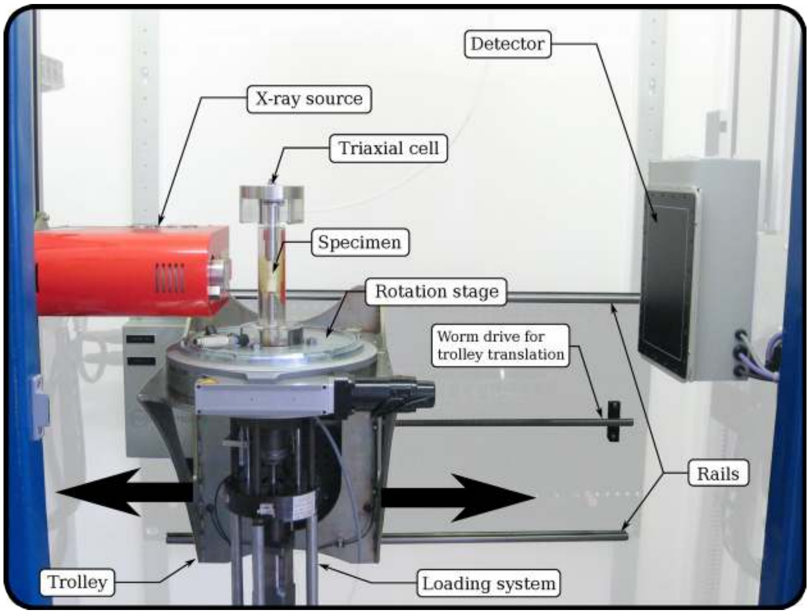

Fig. 3 Labelled photograph of the Laboratoire 3SR x-ray scanner, with background faded out for clarity

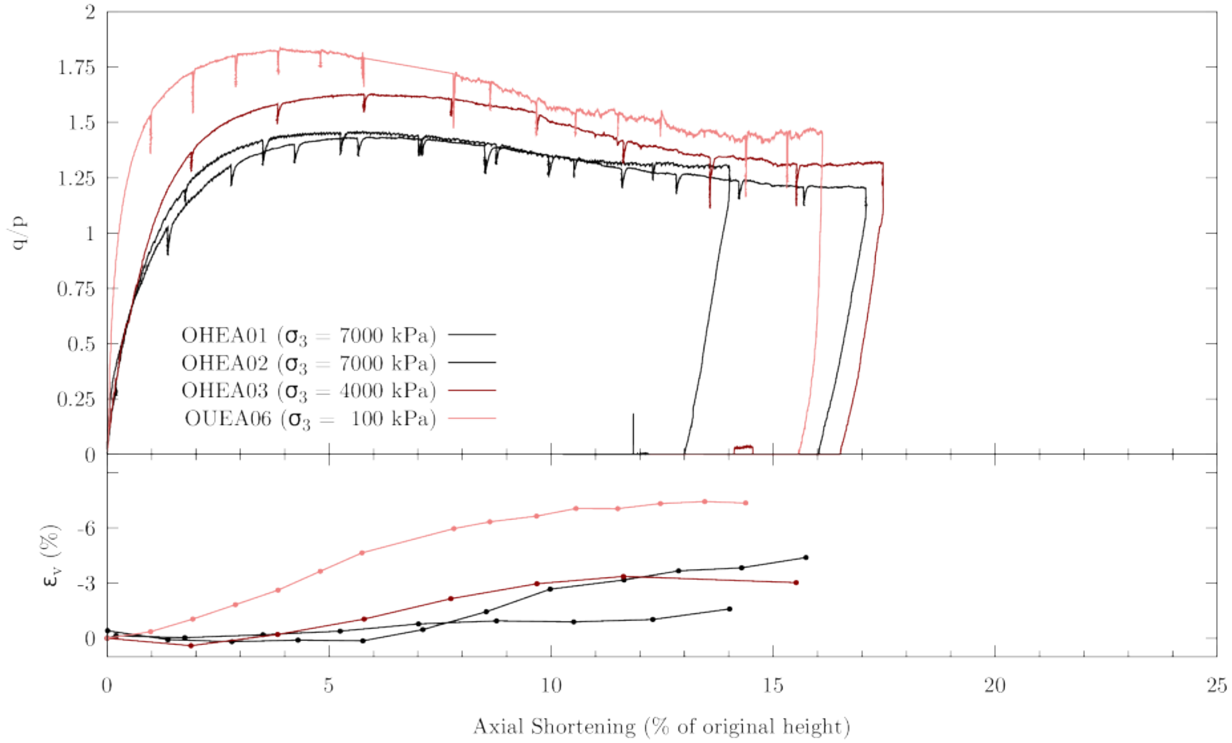

Fig. 4 Deviatoric stress normalised by the mean stress (q/p) vs. axial shortening (top) and volumetric strain vs. axial shortening (bottom) for triaxial compressions tests on Ottawa sand

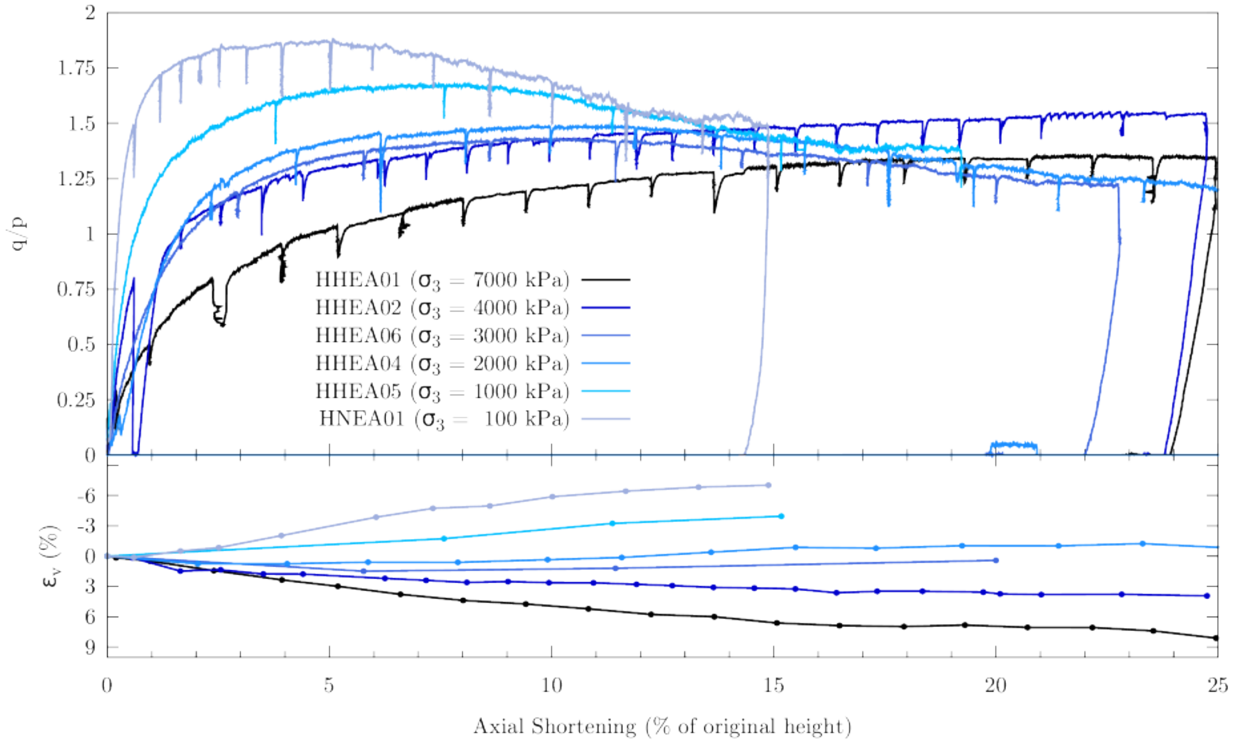

Fig. 5 Deviatoric stress normalised by the mean stress (q/p) vs. axial shortening (top) and volumetric strain vs. axial shortening (bottom) for triaxial compressions tests on Hostun sand

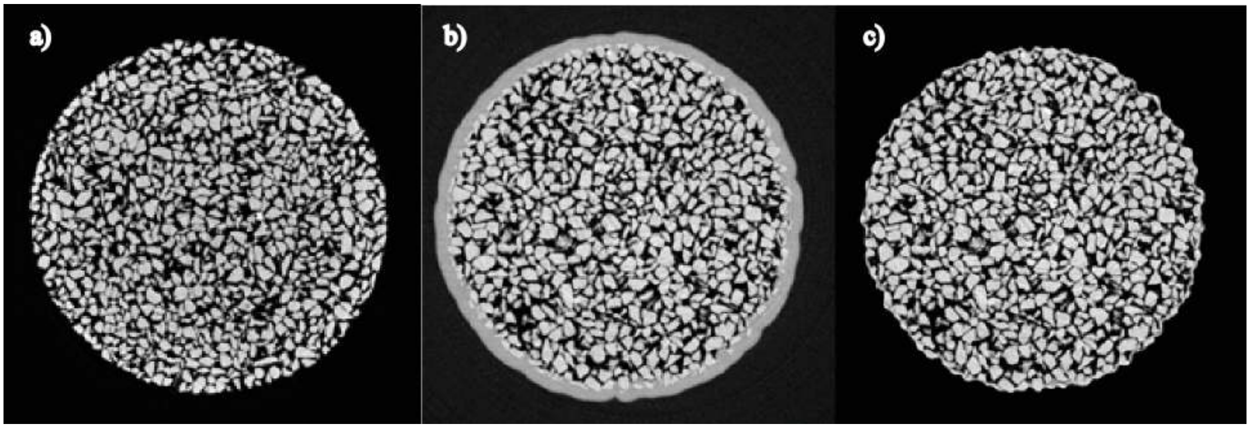

Fig. 6 Horizontal slice of a specimen of Hostun sand a) under low confining pressure, b) and c) under high confining pressure but before and after membrane removal, respectively

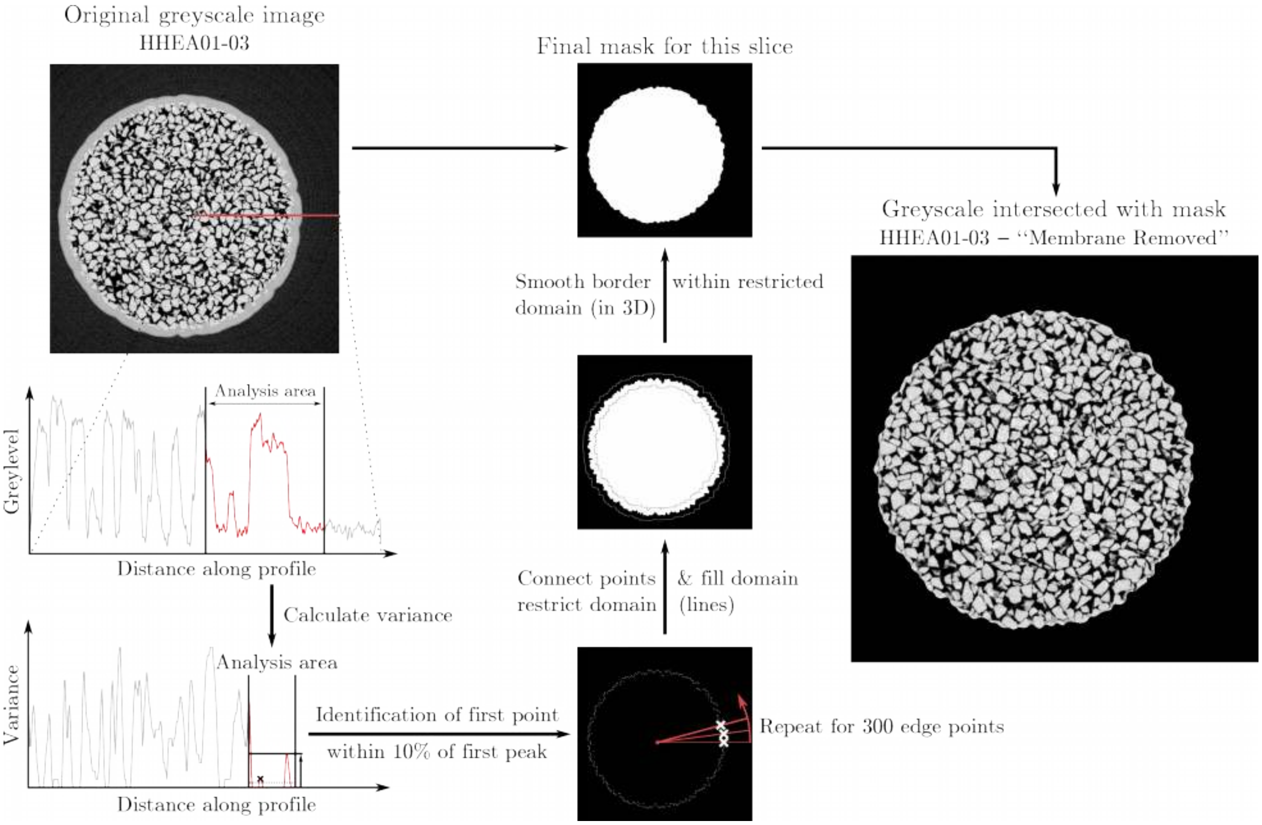

Fig. 7 Illustration of the technique developed for the identification and removal of the membrane from the 3D images acquired with the high pressure cell setup

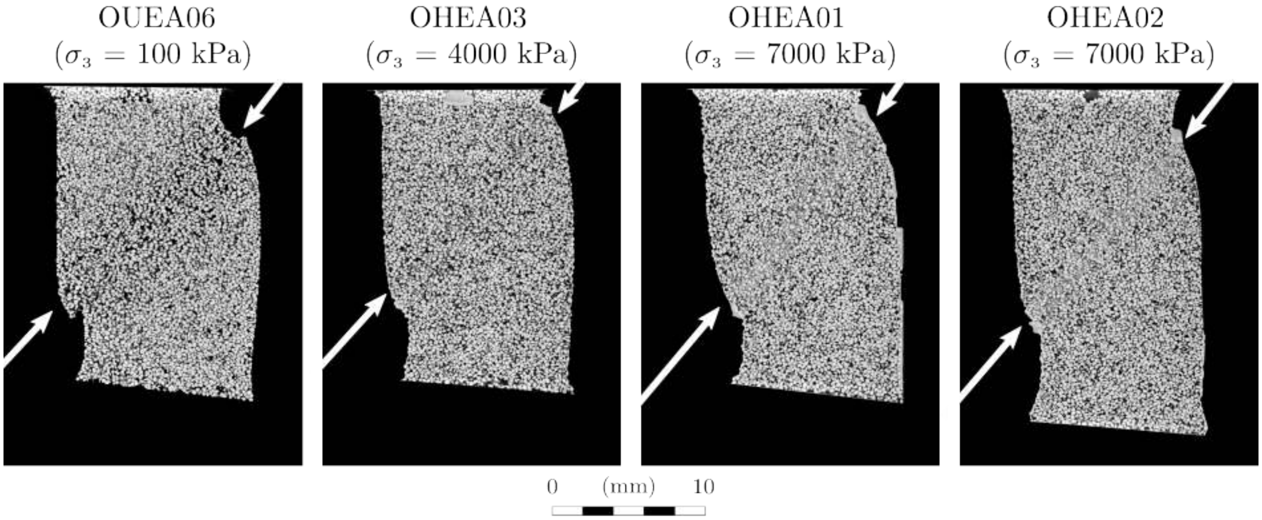

Fig. 8 Vertical slices through the last image acquired in each test on Ottawa sand

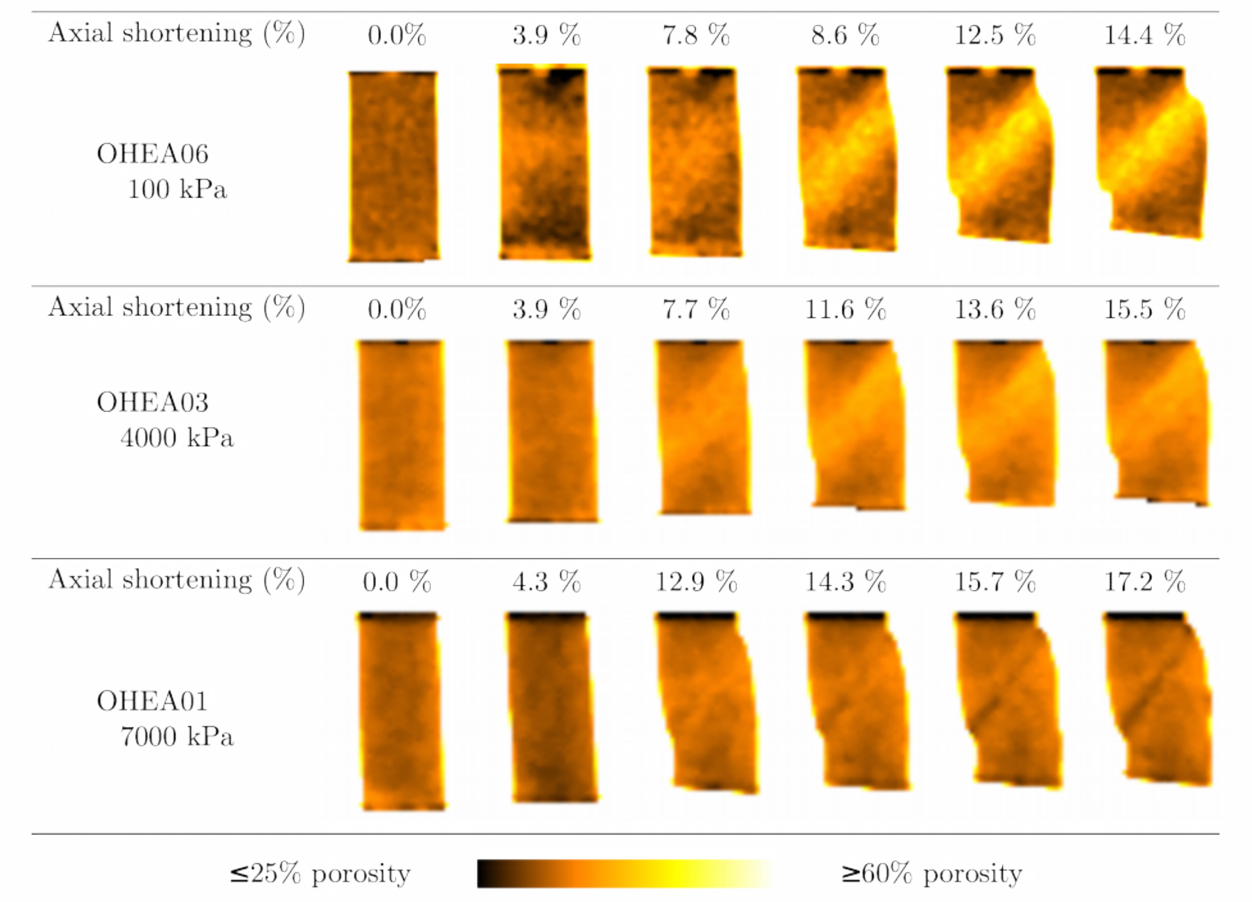

Fig. 9 Porosity maps of some selected states of the specimens of Ottawa sand during shearing

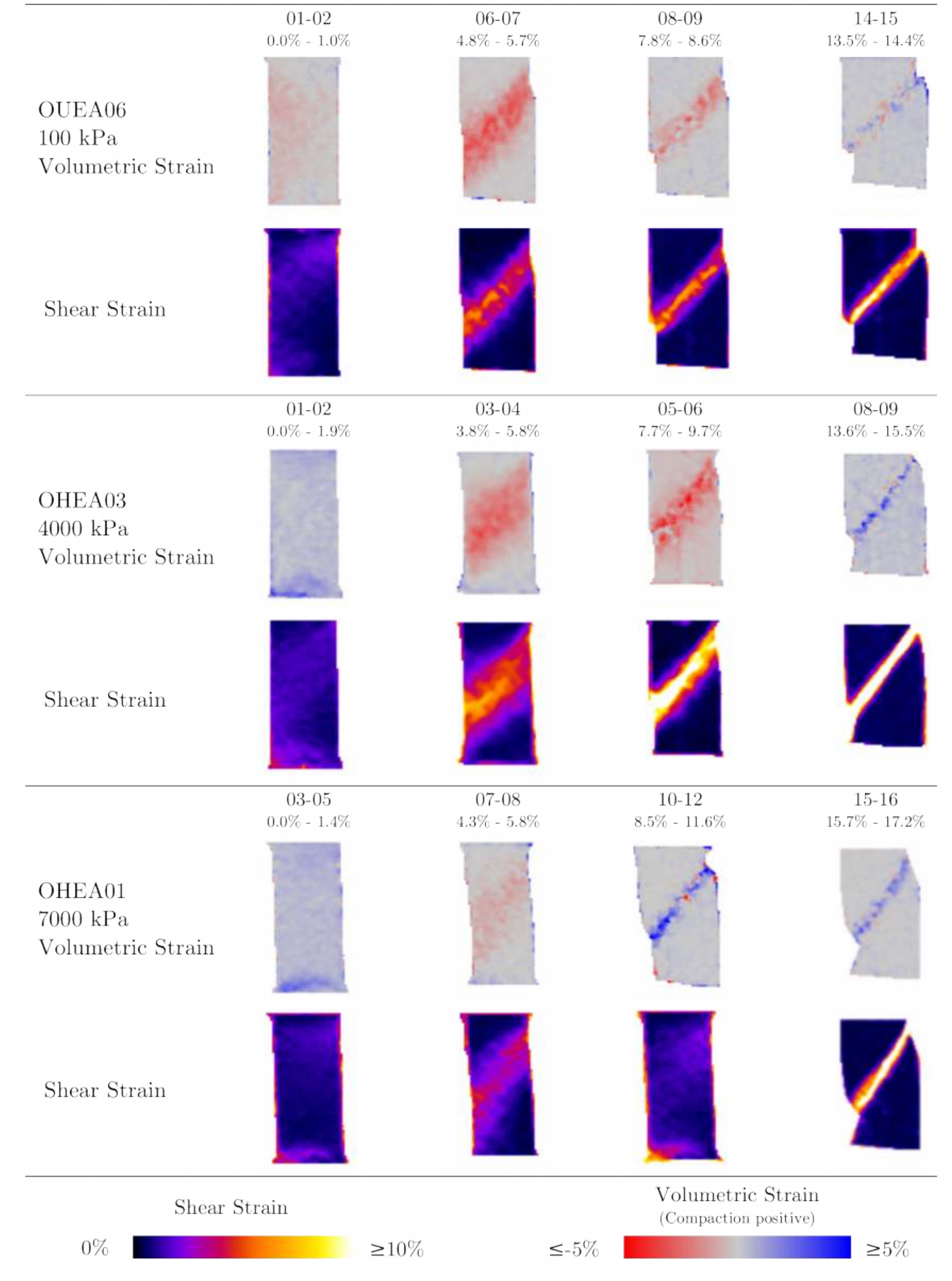

Fig. 10 DIC Results for OUEA06, OHEA03 and OHEA01

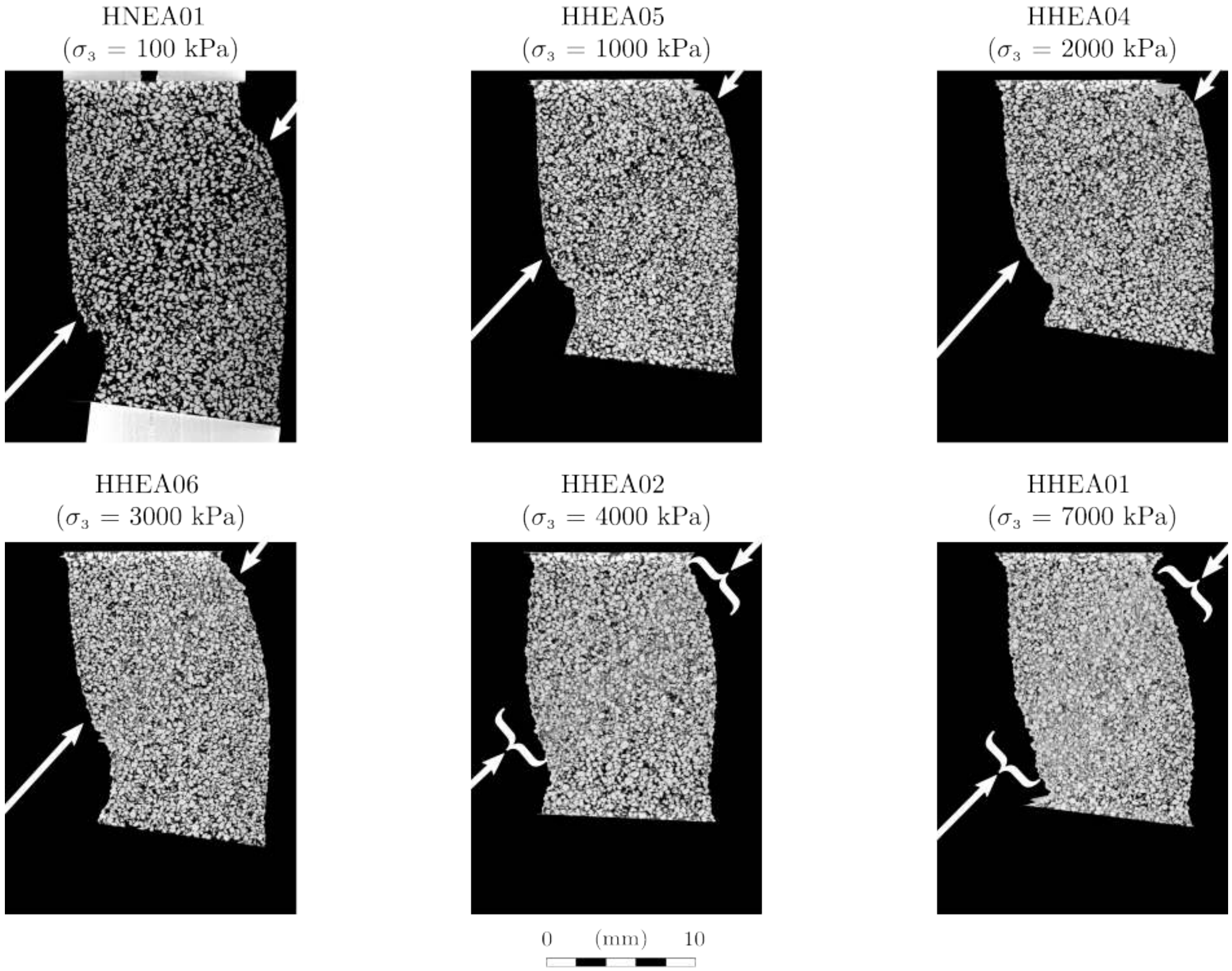
HNEA01 ($\sigma_3 = 100$ kPa)

HHEA05 ($\sigma_3 = 1000$ kPa)

HHEA04 ($\sigma_3 = 2000$ kPa)

HHEA06 ($\sigma_3 = 3000$ kPa)

HHEA02 ($\sigma_3 = 4000$ kPa)

HHEA01 ($\sigma_3 = 7000$ kPa)

Fig. 11 Vertical slices through the last image acquired in each test on Hostun sand

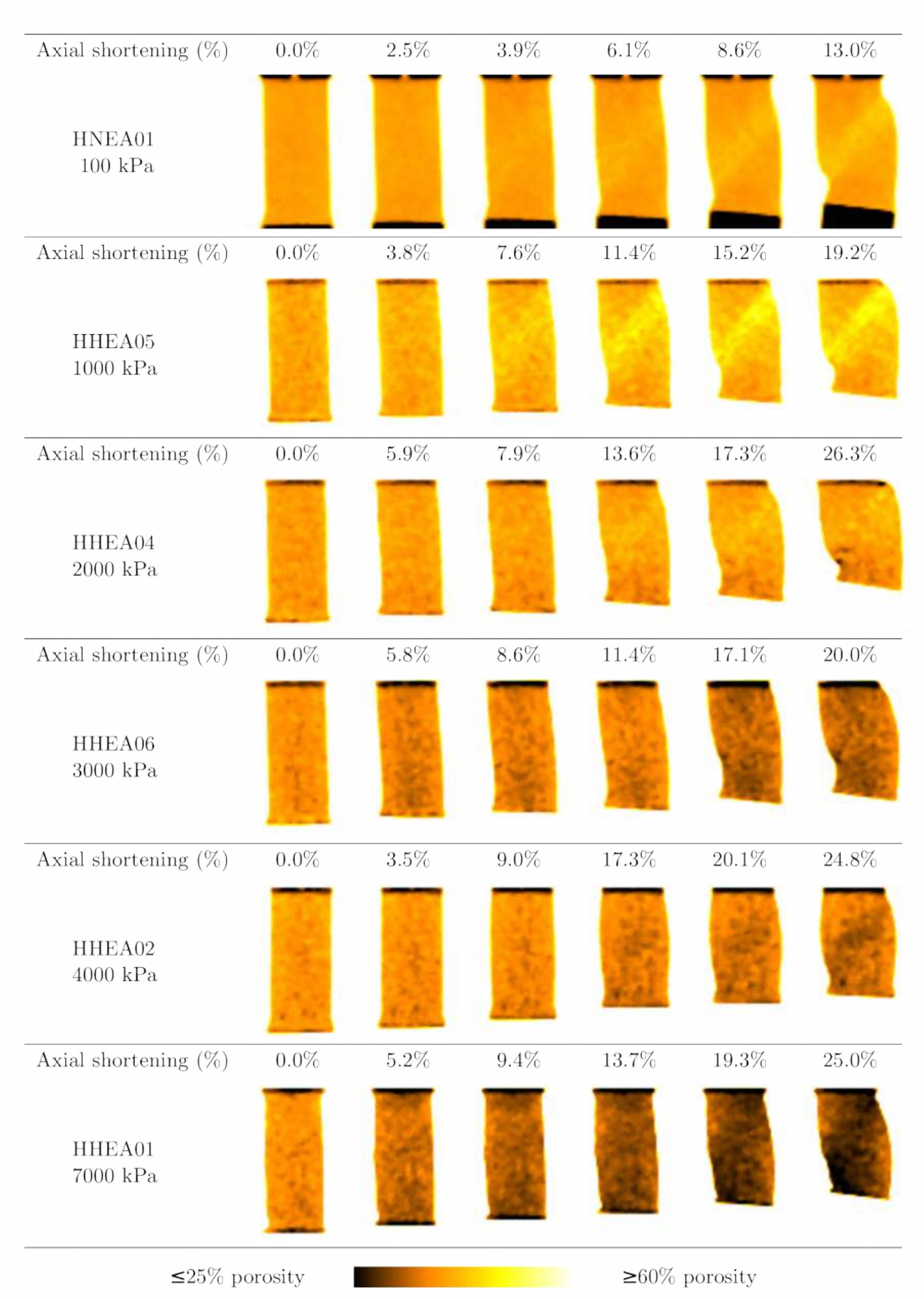

Fig. 12 Porosity maps of some selected states of the specimens of Hostun sand during shearing

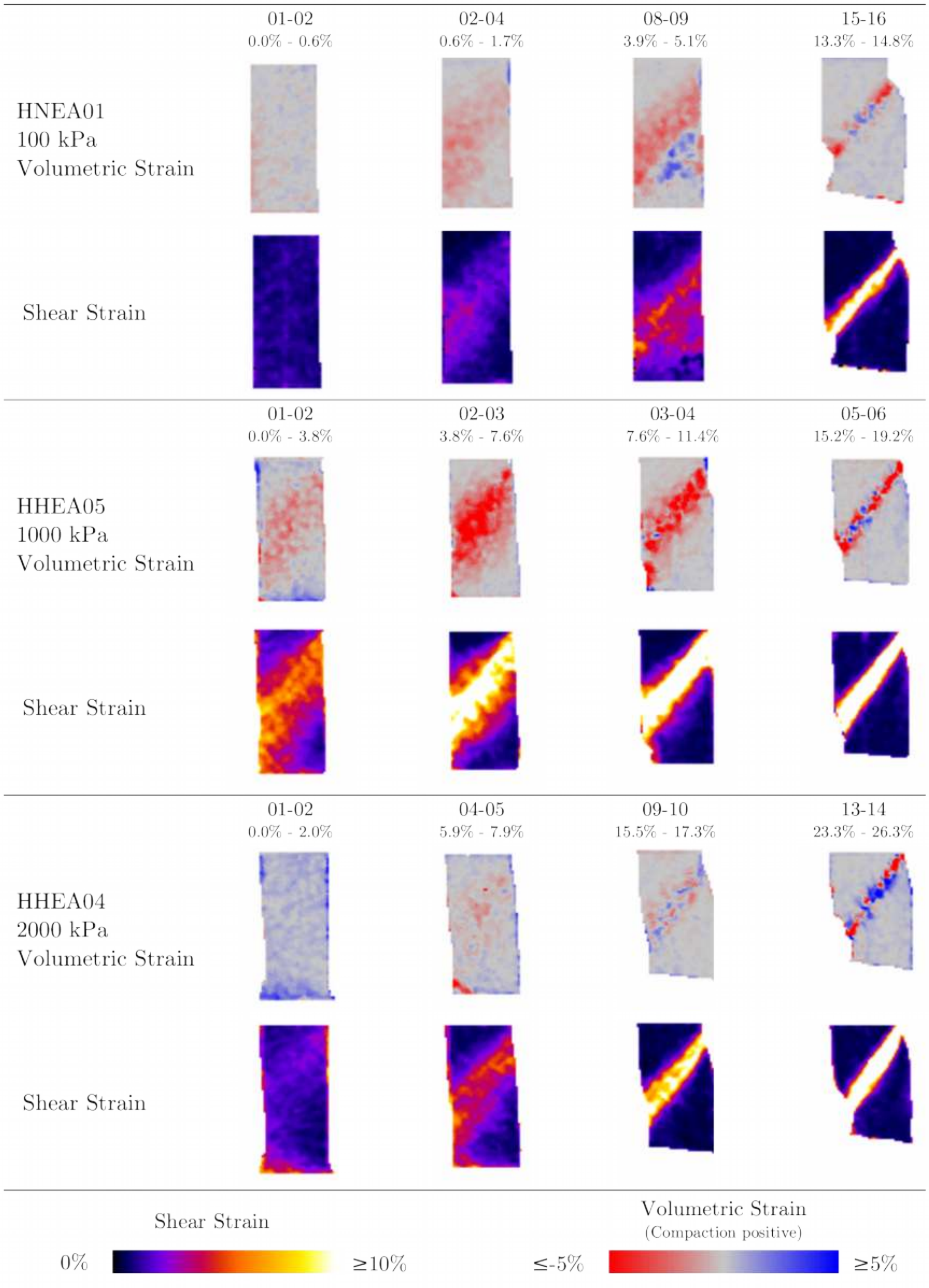

Fig. 13 DIC Results for tests HNEA01, HHEA05 and HHEA04

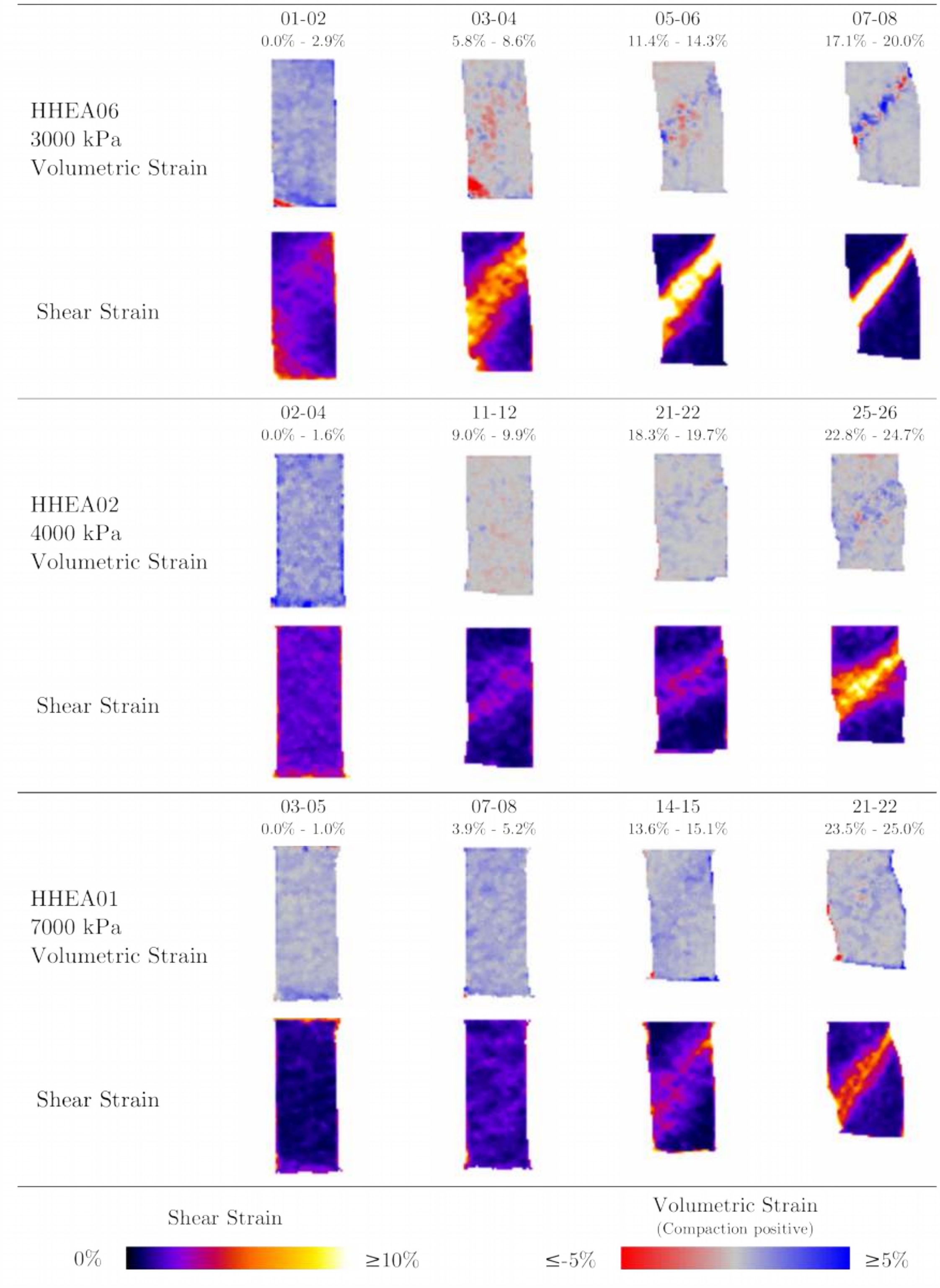

Fig. 14 DIC Results for tests HHEA06, HHEA02 and HHEA01

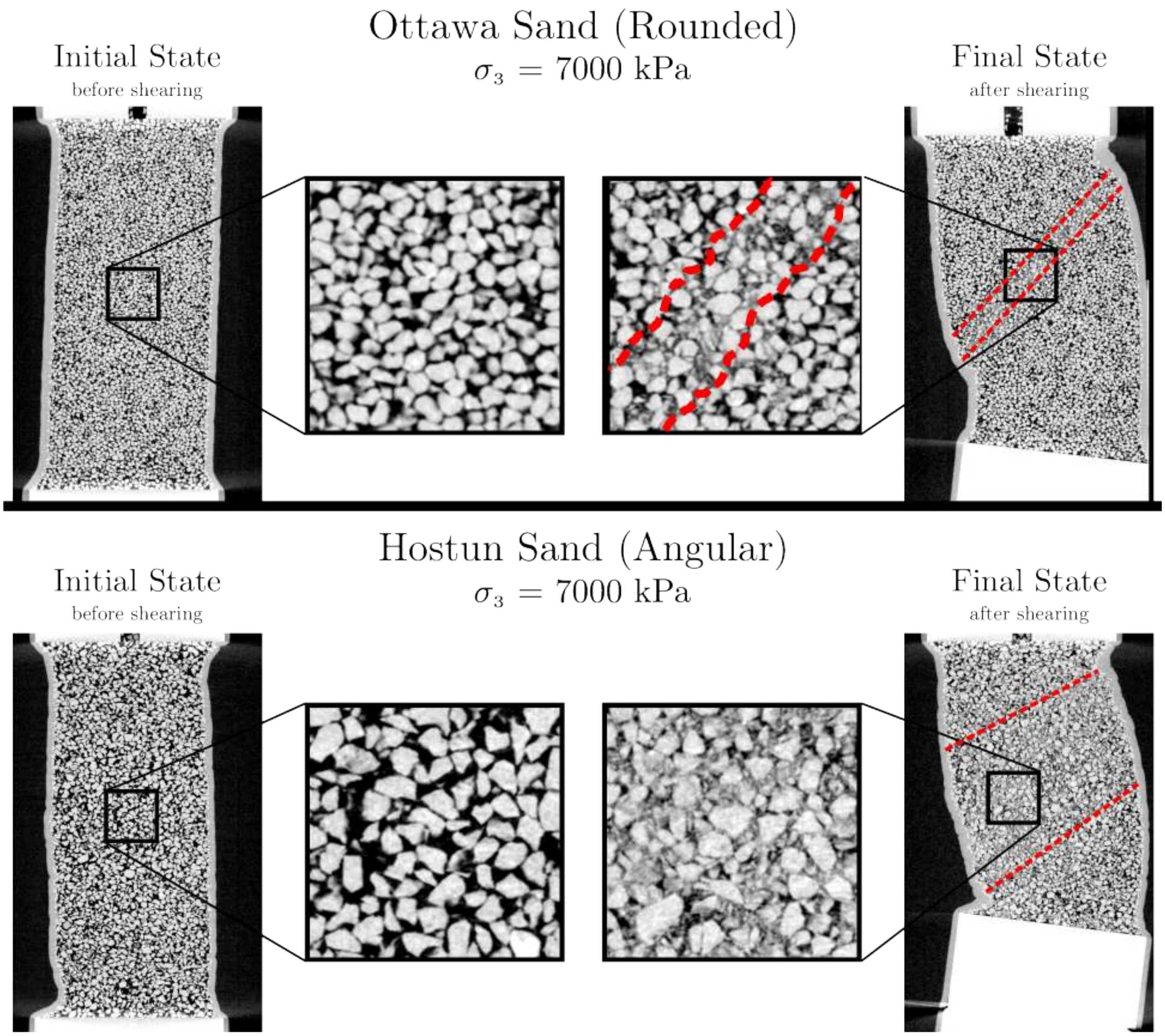

Fig. 15 Vertical sections of Hostun and Ottawa sands (under 7000 kPa confinement) with highlighted zones of intense grain crushing.